CHAPTER 2

*Ag_2S/Bi_2WO_6 NANOCOMPOSITES WITH HIGH PHOTOCATALYTIC ACTIVITY AND STABILITY**

2.1. Introduction

Bi_2WO_6 is one of the simplest member of Aurivillius family which consists of naturally occurring complex layered oxide structures with fluorite-like $(Bi_2O_2)^{+2}$ units alternating with perovskite-like $(A_{m-1}\ B_mO_{3m+1})^{-2}$ blocks, where A = Bi^{+2}, Sr^{+2}, Ba^{+2}, Ca^{+2}, etc., B = W^{+6}, Ta^{+5}, Nb^{+5}, etc., and *m* is the number of BO_6 octahedra in the perovskite-like blocks (*m* = 1–8).[1] The Aurivillius family has numerous members, with $Bi_4Ti_3O_{12}$ (*m* = 3), $SrBi_2Ta_2O_9$ (*m* = 2) and Bi_2WO_6 (*m* = 1) [2–6] being most studied. Bi_2WO_6 is the simplest Aurivillius Oxide with layered structure in which fluorite $Bi_2O_2^{2+}$ layers alternate with perovskite-like slabs of WO_4^{2-} octahedral layers,[7,8] as shown in **Fig. 2.1**.[9]

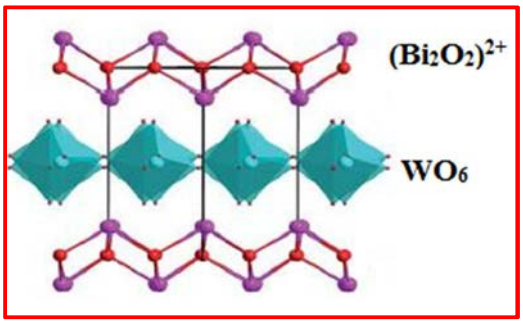

Fig. 2.1: Layered structure of Bi_2WO_6.

Bi_2WO_6 has received considerable attention because of excellent intrinsic physical and chemical properties such as ferroelectricity with spontaneous polarization and high Curie temperature (950°C), catalytic behaviour, piezoelectricity, and non-linear dielectric susceptibility.[10-12] The presence of layered structure in Bi_2WO_6 is considered to promote the generation and separation of charge carriers which makes it an excellent photocatalyst.[13,14] The hybridized valence band (VB) formed by Bi 6s and O 2p levels in Bi_2WO_6 is largely dispersed which enhances the mobility of photohole in the VB.[15] Owing to its non-toxicity and strong oxidizing power, Bi_2WO_6 has been used as one of the promising and excellent photocatalyst for water splitting and decomposition of organic pollutants under visible light.[13,16-18] However, there are still two important factors which limit the photocatalytic efficiency, and thus hinder the practical application of bare Bi_2WO_6 : (1) the absorption edge of pure Bi_2WO_6 is ca, 450 nm[19,20] which overlaps a

*RSC. Adv. 5 (2015) 42910-42921

small part of solar spectrum leading to the unsatisfactory photoresponse range, and hence low photon harvesting efficiency, and (2) the recombination rate of photoinduced charge carriers between the hybrid orbitals of Bi 6s and O 2p to the empty W 5d orbital is high, and therefore, leads to the low quantum efficiency because of the short lifetimes of the electron-hole pairs.[21,22] Therefore, to overcome these drawbacks it is necessary to develop a strategy wherein we could reduce electron-hole recombination and simultaneously broaden the phot-response range of Bi_2WO_6.

2.2. Literature review

It is notable that the photocatalytic activity is closely related to the morphology, size, and structure of photocatalysts.[23,24] For practical applications, the synthesis of Bi_2WO_6 photocatalysts of peculiar structure especially spherical structures composed of ordered nano-substructures with superior visible-light-driven (VLD) photocatalytic activity is a subject of considerable research interest. These nanostructures/superstructures have novel properties which makes them excellent VLD photocatalysts.[25] To improve the photocatalytic activity of bare Bi_2WO_6, many different morphologies of Bi_2WO_6 with different hierarchical architecture and surface area have been reported. These include the development of porous thin films,[26] 3D nest like mesoporous Bi_2WO_6 architectures,[27] nanosized Bi_2WO_6,[28] Bi_2WO_6 hollow nanospheres in water-ethanol mixed solvent,[29] and flower shaped sphere like complex structures.[25,30] Among these, flower shaped Bi_2WO_6 microstructures because of their unique open up like structures have received considerable attention.[25,31-34] For example, Bi_2WO_6 flower-like architectures at low pH with enhanced visible light activity were reported by Wang *et al*.[25] Similarly, CTAB surfactant assisted Bi_2WO_6 flower-like microstructures were developed by Zhang *et al*. through hydrothermal route,[34] and Inorganic salt was used by Qian *et al*.[32] to obtain Bi_2WO_6 flower-shaped microspheres. However, these synthetic procedures were complicated and involved pH value tuning process, and use of surfactants and inorganic salts as templates. In the recent past, green syntheses for the development of photocatalysts have been reported by many researchers.[35-37] 3D Bi_2WO_6 flower-like microstructures assembled from nanoplates with excellent visible-light-driven (VLD) catalytic ability were developed by Zhou *et al*.[38] in a pure water based green reaction system.

Peng *et al*.[39] reported one dimensional (1 D) WO_3-Bi_2WO_6 heterojunctions with superior photocatalytic activity. They reported that (1D) semiconductor structures are potentially high photocatalytic active because they have expected fast transport charge properties,

and in single crystalline nanostructures the expected length scales for minority carrier diffusion are reduced. Various other morphologies of Bi_2WO_6 photocatalyst with better catalytic ability have also been reported.[28,40-43]

Coupling of two photocatalysts to form heterojunction may provide a chance to develop a new photocatalyst with enhanced separation of photoinduced charge carriers and extended photoabsorption range.[44-46] Recent studies have shown that coupling of Bi_2WO_6 with other semiconductors improve the photocatalytic performance of Bi_2WO_6 to a substantial extent by promoting the effective separation of photoinduced charge carriers. Zhang *et al*.[44] developed Bi_2S_3/Bi_2WO_6 composite photocatalyst which exhibited excellent photocatalytic activity than the single Bi_2WO_6 under visible light. Similarly, Ge *et al*.[14] reported Bi_2O_3/Bi_2WO_6 composite with high photocatalytic activity for the degradation of Rhodamine B under visible light. Other composite catalysts with superior photocatalytic ability than bare Bi_2WO_6 include α-Fe_2O_3/Bi_2WO_6,[47] TiO_2 modified flower like Bi_2WO_6,[48] Bi_2WO_6/BiOBr,[49] WO_3-Bi_2WO_6,[39] CuPc sensitized Bi_2WO_6,[50] AgBr quantum dots decorated mesoporous Bi_2WO_6,[51] Ag-AgBr-Bi_2WO_6,[52] Ag-graphene/Bi_2WO_6,[53] Bi_2CO_3 decorated Bi_2WO_6 nanosheets,[54] carbon modified Bi_2WO_6,[55] $BiIO_4/Bi_2WO_6$ heterojunctions,[56] Bi_2WO_6@$CaWO_4$,[57] mesoporous Carbon/Bi_2WO_6,[58] and $PtCl_4/Bi_2WO_6$.[59]

2.3. Present work

As widely accepted, an efficient photocatalyst should have high mobility of photogenerated charges and extended photoabsorption range to maximally utilize the sunlight energy.[60] As discussed above, the coupling of two semiconductors is considered as an effective strategy towards extending the visible light spectral responsive range and facilitating the effective separation of photogenerated charges.[61-63] Previously organic dye sensitizers have been used in Dye sensitized cells (DSSC) to increase the utilization rate of solar energy.[64,65] Similarly Zhang *et al*. synthesized a composite photocatalyst by introducing copper phthalocyanin (CuPc) into Bi_2WO_6.[50] The introduction of CuPc lead to the enhancement of photoabsorption property of Bi_2WO_6, and the composite catalyst showed photo-response in the entire visible region. Inspired by all these results, a composite photocatalyst Ag_2S/Bi_2WO_6 was fabricated by us to exploit longer wavelength part of visible spectrum, and to enhance the effective separation of photoinduced charge carriers.

Ag_2S is an important chalcogenide with a narrow band gap of 1.1 eV, and has been investigated extensively for the numerous applications such as photovoltaic device

construction,[66,67] photocatalytic decomposition of organic pollutants,[68,69] and photocatalytic H_2 production.[70] Moreover, Ag_2S has high absorption coefficient[70-75] and is also free from toxic heavy elements like Pb and Cd, and thus possess negligible toxicity compared to other narrow band gap materials.[76] Owing to the high chemical stability, narrow band gap, high absorption coefficient, and excellent optical limiting properties of Ag_2S, it was coupled with Bi_2WO_6 to form a heterojunction with enhanced visible light photocatalytic activity and high stability.

The photocatalytic activity of the as prepared Ag_2S/Bi_2WO_6 photocatalyst was evaluated by decomposing the dye Rhodamine B. The effect of Ag/Bi weight ratio on the photocatalytic activity was also studied. The photocatalytic experiment was performed in an immersion well reactor. The as synthesized composite system exhibited superior visible light induced photocatalytic activity than bare Bi_2WO_6. Scavenger experiments and terepthalic acid (TA) fluorescence experiments were carried out to investigate the primary reactive species involved in the photocatalytic decolourization of dye. Photoluminescence (PL) analysis was used to confirm the effective separation of photoinduced charge carriers. The stability of the photocatalyst which is a major concern for catalysts containing silver was also investigated by repetition experiments. The used catalyst was analysed with XRD and XPS technique to assure that no metallic silver is formed during photocatalytic oxidation (PCO) process.

2.4. Experimental

2.4.1. Synthesis of Ag_2S-Bi_2WO_6 photocatalyst

The hierarchical structures of Ag_2S/Bi_2WO_6 were synthesized by a two-step process. In the first step, the mesoporous Bi_2WO_6 microspheres were fabricated by a simple solvothermal process *via* following procedure: 1 mmol of $Na_2WO_4.2H_2O$ was dissolved in 15 mL of ethylene glycol under constant stirring. Then 2 mmol of $Bi(NO_3)_3.5H_2O$ was added into the solution and the mixture was stirred for 20 min. Thereafter, absolute ethanol (25 mL) was added into the solution and the suspension was transferred into a 50 mL Teflon-lined stainless steel autoclave, and heated at 180 °C for 24h. The autoclave was subsequently cooled to room temperature. The products were collected by filtration. The as obtained products were washed with de-ionized water and absolute ethanol for several times, and then dried at 80 °C for 12h.

In the second step, impregnation of Bi_2WO_6 surface with Ag_2S was carried out by *in-situ* growth of Ag_2S on Bi_2WO_6 substrate at room temperature. In a typical experimental procedure, 0.6 g of Bi_2WO_6 microspheres and different amounts of $AgNO_3$ were

dispersed in 50 mL of absolute ethanol, and ultrasonicated for 30 min. After ultrasonication, appropriate amount of Na_2S was added to the suspension with continuous stirring. The obtained suspension was vigorously stirred for 8 h. The precipitates were collected and washed with de-ionized water and absolute ethanol for several times, and then dried at 80 °C for 12h. The different weight ratios of Ag_2S to Bi_2WO_6 samples were prepared and noted as 3% Ag_2S/Bi_2WO_6, 5% Ag_2S/Bi_2WO_6, 7% Ag_2S/Bi_2WO_6, and 9% Ag_2S/Bi_2WO_6. For comparison pure Ag_2S was also synthesized in absence of Bi_2WO_6.

2.4.2. Characterization

To examine the phase purity and crystal structure of as prepared samples, XRD analysis was carried out using a PANalytical, XPert PRO powder X-ray diffractometer with CuKα radiation (λ= 1.5418 A°) having a tube voltage of 40kV and current of 30 mA at room temperature with the scan range 2θ = 15 to 80° and step size 0.02666°. X-ray photoelectron spectroscopy (XPS) was used to analyse the surface properties of samples using MK II photoelectron spectrometer having Al-K(alpha) (1486.6 eV) as the X-ray source. The particle morphology and microstructure of the samples was investigated by FESEM using Carl-Zeiss field-emission scanning electron microscope (FESEM) equipped with EDS attachment, and transmission electron microscopy (TEM) using JEOL, JEM 2100F instrument. UV-vis DRS spectra of samples in the region of 300-800 nm was recorded by UV-vis NIR spectrometer (Perkin Elmer) equipped with an integrating sphere assembly. The surface area and pore size distribution of the as prepared samples was characterized by N_2 adsorption-desorption isotherm using Quantachrome Instruments Autosorb 1C. Adsorption of samples was done at 77 K. The samples were degassed at 150 ^oC for 3 h before analysis. Photoluminescence (PL) spectra were recorded on Flourospectrometer.

2.4.3. Photocatalytic activity

To evaluate the photocatalytic activity of the samples, RhB and phenol aqueous solutions were degraded under visible light irradiation. A 500 W, tungsten halogen lamp was used as the light source. Immersion well photoreactor made of pyrex glass was used to perform the experiments. Refrigerated circulating liquid bath was used to keep the temperature of the reaction constant at 20 ± 0.3 °C. The experiments were performed as follows: 0.18 g of the as prepared catalyst was added into 180 mL RhB aqueous solution. Prior to the illumination, the suspension was magnetically stirred for at least 30 min in the dark to attain adsorption-desorption equilibrium between dye and catalyst. 5mL suspensions were sampled at 5 min time intervals, and then centrifuged to remove the catalyst particles. The

concentration of catalyst free dye solution was analysed at λ_{max} (554 nm) using Shimadzu UV–vis 1601 spectrophotometer.

To determine the effect of scavengers on photocatalytic activity, appropriate quantity of scavenger species were introduced in the reaction system in a manner similar to photocatalytic experiment. Photoluminescence (PL) technique with Terepthalic acid (TA) as a probe molecule was used for the detection of $^{\bullet}OH$ radicals. The experimental procedure was referred to previous studies.[45]

2.5. Results and discussions

2. 5.1. XRD analysis

XRD analysis was used to determine the purity, phase structure, and crystallinity of the as prepared samples. **Fig. 2.2** presents the XRD pattern of pristine Bi_2WO_6 and Ag_2S loaded Bi_2WO_6.

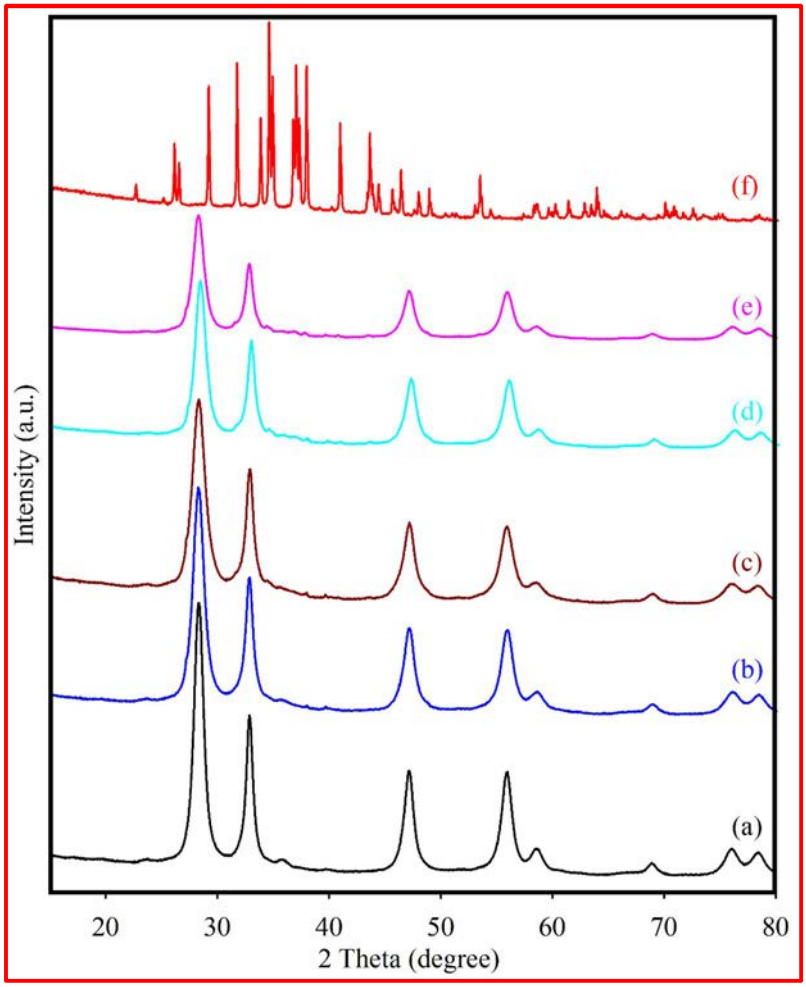

Fig. 2.2: XRD patterns of: (a) the pure Bi_2WO_6, (b) the 3% Ag_2S/Bi_2WO_6 catalyst, (c) the 5% Ag_2S/Bi_2WO_6 catalyst, (d) the 7% Ag_2S/Bi_2WO_6 catalyst, (e) the 9% Ag_2S/Bi_2WO_6 catalyst, and (f) the pure Ag_2S.

As can be seen from the **Fig. 2.2 (a)**, the diffraction peaks can be categorised into a set of 2θ at 28.3°, 32.8°, 47.1°, and 55.9° corresponding to the indices (131), (200), (202), and (331) which indicates a perfectly orthorhombic structure for pure Bi_2WO_6.[51] Compared with diffraction pattern of bare Bi_2WO_6, the characteristic absorption peaks associated with Ag_2S are not obviously detected in Ag_2S/Bi_2WO_6 composites **(Fig. 2.2 (b-e))**. This may be due to the limited amount of Ag_2S (3% - 9%) used, small size of Ag_2S nanoparticles, and high dispersion of Ag_2S on the surface of Bi_2WO_6 spherical architectures. More importantly, the absence of individual Ag_2S aggregates in SEM images of as prepared samples indicate high dispersion of Ag_2S in composites. **Fig. 2.2 (f)** displays the characteristic XRD pattern of pure Ag_2S sample. All peaks of pure Ag_2S can be assigned to monoclinic Ag_2S crystal structure[77]. The average crystallite size of the samples was calculated by using Scherer formula[45] **(Equation 2.1)** and results are listed in **Table 2.1**.

$$D = {}^{k\lambda}/_{\beta Cos\theta} \qquad [2.1]$$

Where D is taken as crystallite size, k is a constant, λ is X-ray wavelength, β is the full width at half maximum (FWHM) measured in radians on the 2θ scale, and θ is the Bragg angle for diffraction peaks. From the results of crystallite size displayed in **Table 2.1**, it is clear that there is negligible difference in the crystallite size of pure Bi_2WO_6 and Ag_2S loaded Bi_2WO_6 samples.

Table 2.1. Average crystallite size of Bi_2WO_6 and Ag_2S/Bi_2WO_6 hybrids.

Sample	Average Crystallite size (nm)
Bi_2WO_6	11.12
3% Ag_2S/Bi_2WO_6	11.28
5% Ag_2S/Bi_2WO_6	10.56
7% Ag_2S/Bi_2WO_6	10.66
9% Ag_2S/Bi_2WO_6	11.42

2.5.2. XPS analysis

To further investigate the composition and oxidation states of as prepared samples, the XPS analysis of 7% Ag_2S/Bi_2WO_6 heterostructure **(Fig. 2.3)** was carried out. **Fig. 2.3 (a)** displays the overall XPS spectra for the 7% Ag_2S/Bi_2WO_6 in which peaks for Bi, W, O, Ag, and S can be detected. The high resolution XPS spectra of Bi4f, W4f, O2S, S2p, and Ag3d is shown in **Fig. 2.3 (b-f)**. The Bi4f peaks **(Fig. 2.3 (b))** at 157.8 eV and 163.10 eV

are attributed to the binding energies of $Bi4f_{7/2}$ and $Bi4f_{5/2}$ respectively, which correspond to previous results.[78] The W4f peaks at 34.00 eV and 36.1 eV are ascribed to binding energies of $4f_{7/2}$ and $4f_{5/2}$ **(Fig. 2.3 (c))**. The splitting energy of 2.1 eV for 4f doublet of W indicate the +6 oxidation state of W in composite catalyst.[79] The O1S peak **(Fig. 2.3 (d))** at 528.8 eV is in good agreement with previous results.[78] The high resolution Ag3d XPS spectrum is displayed in **Fig. 2.3 (e)**. The two peaks corresponding to Ag^+ at approximately 366.50 eV and 372.60 eV are attributed to the $Ag3d_{5/2}$ and $Ag3d_{3/2}$ respectively.[80] Since in previous results, the peaks at 368.3 and 374.2 eV are attributed to metallic Ag, whereas the peaks at 367.8 and 373.8 eV are attributed to Ag^+,[81,82] it implies that peaks obtained in our XPS results can be ascribed to Ag^+ only suggesting that no metallic Ag^0 is formed. **Fig. 2.3 (f)** displays the S2P XPS spectrum. The peak at around 163 eV can be attributed to $S2P_{1/2}$ indicating the presence of S^{2-}, which further suggests the formation of Ag_2S.[83] Therefore, it can be confirmed from these results that Ag_2S/Bi_2WO_6 composites have been successfully synthesized.

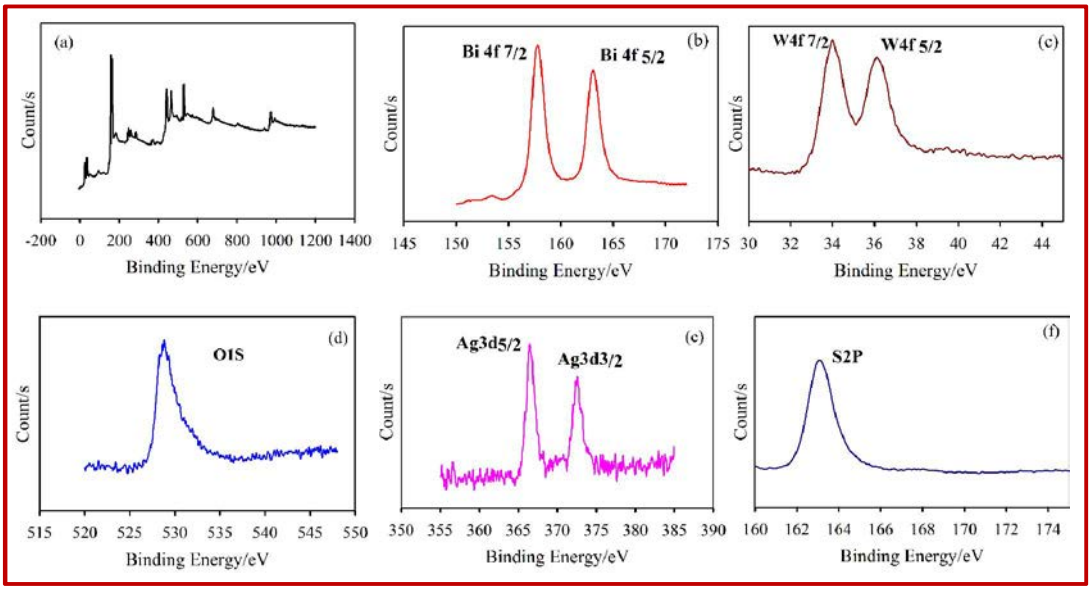

Fig. 2.3: XPS spectra of 7% Ag_2S/Bi_2WO_6: (a) Full survey spectra, and high resolution XPS spectra of the sample: (b) Bi 4f, (c) W 4f, (d) O 1s, (e) Ag 3d, and (f) S 2p.

2.5.3. SEM, EDS and TEM analysis

To investigate the surface morphology of as prepared samples, SEM characterization was used. **Fig. 2.4** presents the FESEM images of pure Bi_2WO_6 and 7% Ag_2S/Bi_2WO_6 composite. As clear from the **Fig. 2.4 (a)**, the FESEM image of bare Bi_2WO_6 consist of abundant hierarchically structured architectures of Bi_2WO_6 microspheres. The higher magnification **(Fig. 2.4 (b))** reveals that Bi_2WO_6 architectures are built from numerous nanoplates aligned to the spherical surface forming a microsphere. Compared to bare

Bi_2WO_6, the Ag_2S loading affects the surface morphology of Bi_2WO_6 in composite system to some extent **(Fig. 2.4 (c))**. As can be seen clearly from the higher magnification FESEM image of 7% Ag_2S/Bi_2WO_6 composite **(Fig. 2.4 (d))**, it is somewhat different from spherical structure showing that Ag_2S has combined well with Bi_2WO_6 to form a heterostructure.

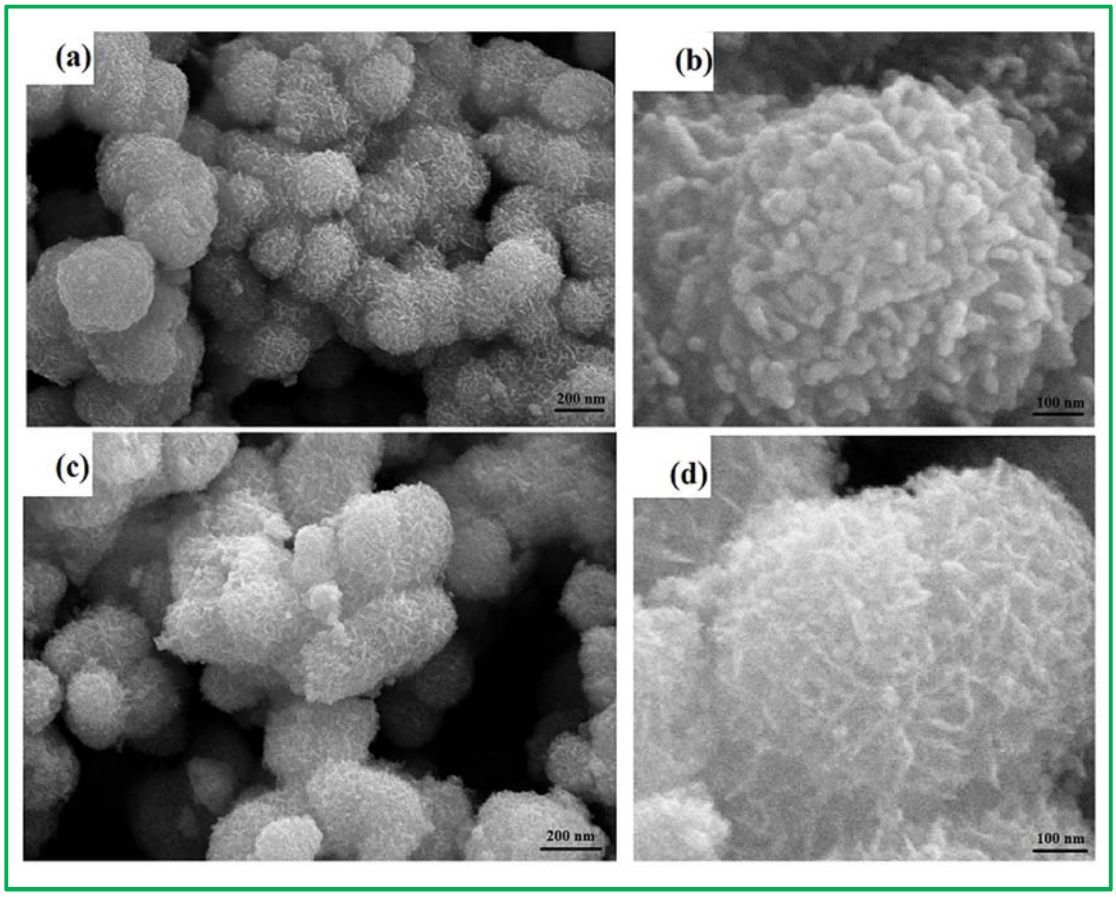

Fig. 2.4: FE-SEM images of samples: (a) Pure-Bi_2WO_6, (b) the high magnification SEM image of Pure Bi_2WO_6, (c) 7% Ag_2S/Bi_2WO_6, and (d) the high magnification SEM image of 7% Ag_2S/Bi_2WO_6.

EDS spectrum of Bi_2WO_6 and 7% Ag_2S/Bi_2WO_6 was collected to confirm the presence of Ag_2S in hybrids. The EDS spectrum in **Fig. 2.5 (a)** shows clearly that bare Bi_2WO_6 is composed of Bi, W, and O elements, whereas Ag_2S/Bi_2WO_6 composite **(Fig. 2.5 (b))** is composed of Bi, W, O, Ag, and S elements indicating the formation of Ag_2S/Bi_2WO_6 composite. To further confirm the high dispersion of Ag_2S in composite, the EDS elemental mapping of 7 % Ag_2S/Bi_2WO_6 composite was performed as shown in **Fig. 2.6**. It can be seen from the **Fig. 2.6**, that Ag **(Fig. 2.6 (b))** and S **(Fig. 2.6 (e))** are highly dispersed in 7% Ag_2S/Bi_2WO_6 hybrid.

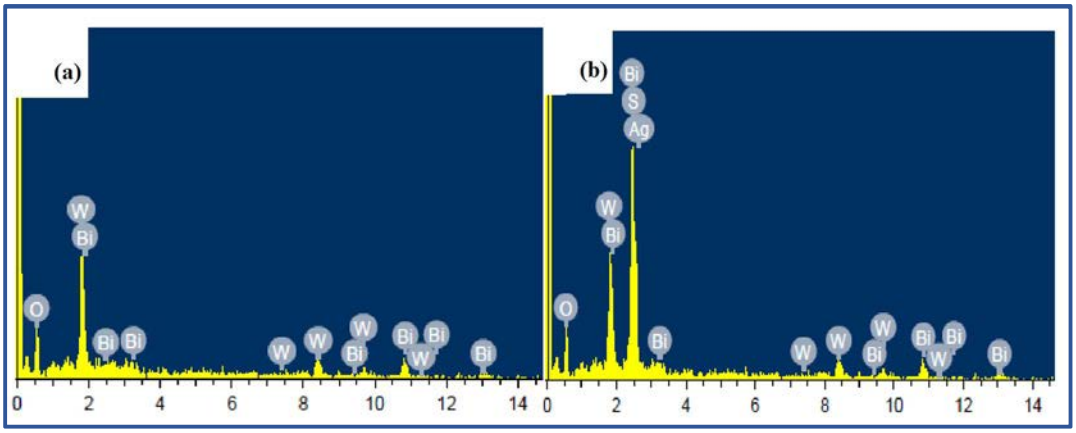

Fig. 2.5: (a) EDS spectrum of Pure-Bi_2WO_6 sample, and (b) EDS spectrum of 7% Ag_2S/Bi_2WO_6 sample.

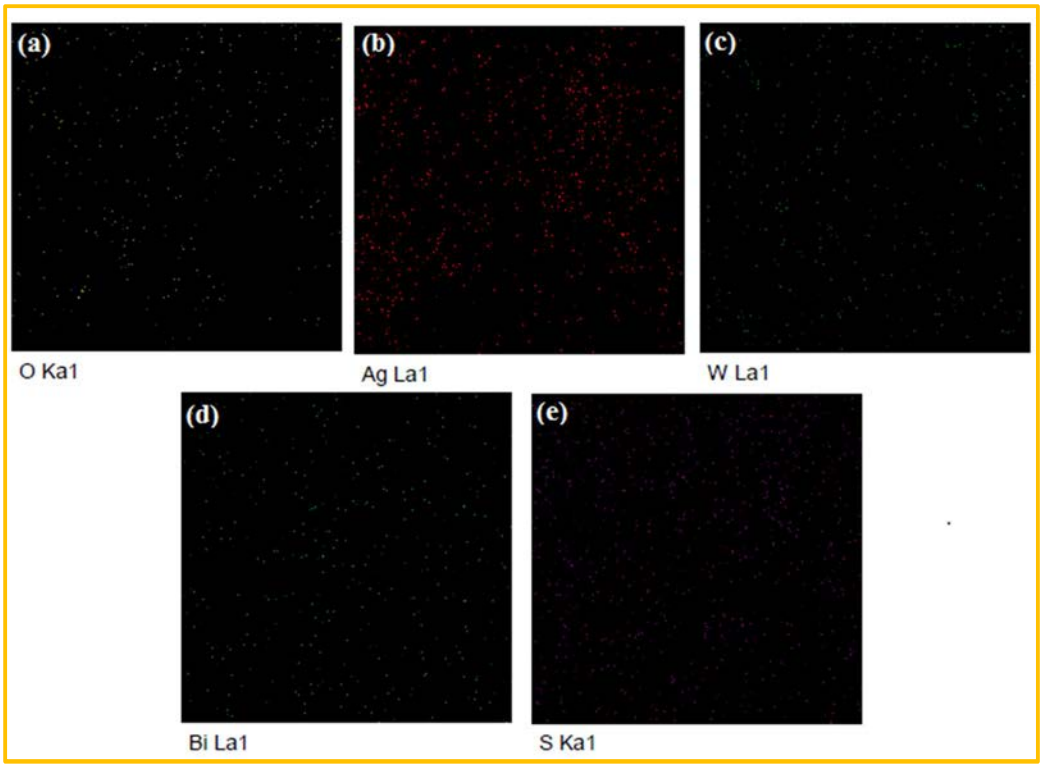

Fig. 2.6: EDS elemental mapping of 7% Ag_2S/Bi_2WO_6.

TEM analysis was further used to investigate the detailed structure, as shown in **Fig. 2.7**. It can be seen that Bi_2WO_6 structures are composed of nanoplates with a thickness of around 10-20 nm **(Fig. 2.7 (a))**. **Fig. 2.7 (b)** shows that Bi_2WO_6 microspheres are mesoporous in nature which helps Ag_2S particles to bind in this composite system. The TEM image for 7% Ag_2S /Bi_2WO_6 **(Fig. 2.7 (d and e))** shows subtle particles of Ag_2S grown on the surface of Bi_2WO_6 microsphere. The presence of lattice fringes **(Fig. 2.7 (c))** confirms the crystalline nature of Bi_2WO_6. Furthermore, the spacing of lattice fringes is found to be 0.313 nm which corresponds to the 131 planes of orthorhombic Bi_2WO_6.[51]

All these results are in good agreement with the results of XRD and XPS analysis, and strongly demonstrate the formation of Ag_2S/Bi_2WO_6 heterojunction.

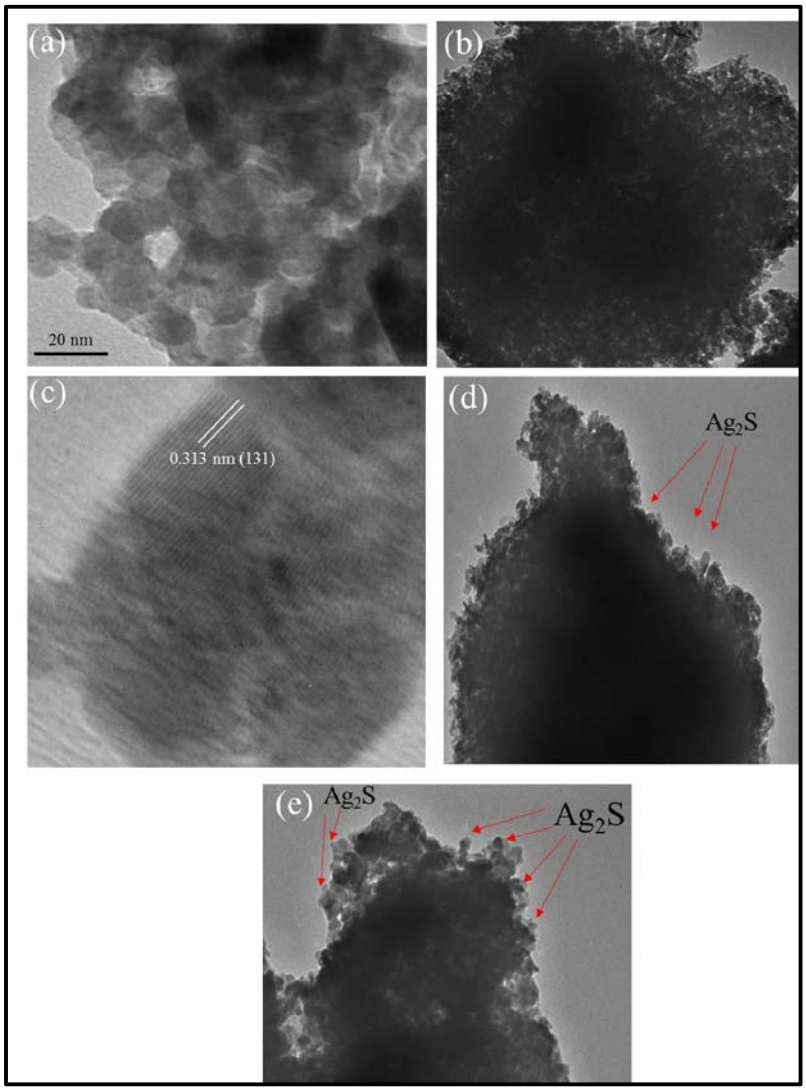

Fig. 2.7: TEM images of samples: (a and b) Pure Bi_2WO_6, (d and e) 7% Ag_2S/Bi_2WO_6.

2.5.4. N_2 Adsorption-Desorption

Fig. 2.8 shows the nitrogen adsorption isotherm and pore size distribution of pure Bi_2WO_6 **(Fig. 2.8 (a))** and 7% Ag_2S/Bi_2WO_6 **(Fig. 2.8 (b))**. It is evident from the figure that the shape of both the isotherms seem to be nearly of type IV isotherm with hysteresis loop at higher relative pressure, which is usually associated with capillary condensation in mesopores.[84 85] The type H3 hysteresis loop at higher relative pressure according to IUPAC classification reflects the presence of slit like pores indicating the presence of mesopores in the region of 2-10 nm which is further confirmed by the BJH pore size distribution diagram in the inset of **Fig. 2.8**.

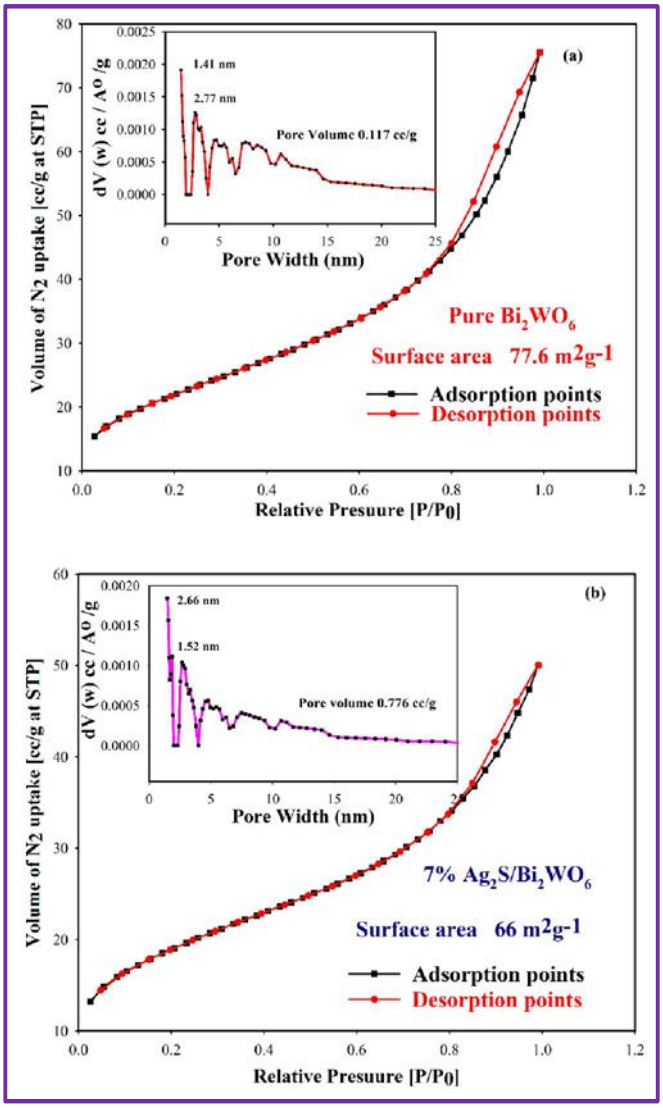

Fig. 2.8: N_2 adsorption-desorption isotherm of the samples (a) Pure Bi_2WO_6 and (b) 7% Ag_2S/Bi_2WO_6. The insets are the pore size distribution of the respective catalysts.

2.5.5. Optical properties

Fig. 2.9 displays the UV-vis diffuse reflectance (DRS) spectra of bare Bi_2WO_6 and Ag_2S/Bi_2WO_6 heterostructures. As shown in **Fig. 2.9 (a)**, the bare Bi_2WO_6 has an absorption edge around 450 nm whereas weak and broadened peaks of Ag_2S **(Fig. 2.9 (b))** are similar to the reported UV-vis spectra of pure Ag_2S.[86, 87] With increase in Ag_2S loading, the absorption edge of heterostructure samples shifts to longer wavelengths from 450-490 nm.

The optical band gaps (insets of **Fig. 2.9 (a)** and **Fig. 2.9 (b)**) of Bi_2WO_6 and Ag_2S were calculated using the **Equation 2.2**, reported by Butler.[88]

$$h\nu.\alpha = (A h\nu - E_g)^{n/2} \qquad [2.2]$$

Since α is proportional to Kubelka - Munk Function F(R), the equation becomes

$$h\nu.F(R) = (A h\nu - E_g)^{n/2} \qquad [2.3]$$

Where h is the Planck's constant, ν is the frequency, A is the proportionality constant, and E_g is the band gap energy. The value of 'n' is determined by the type of transition (n = 1 for direct and n = 4 for indirect transition). The 'n' for Bi_2WO_6 has been reported by some researchers as 1 (direct transition)[89,90] and by some other researchers as 4 (indirect transition)[91,92]. In our case we plotted $(F(R).h\nu)^{1/2}$ versus $h\nu$ for Bi_2WO_6 (inset of **Fig. 2.9 (a)**) and $(F(R).h\nu)^2$ versus hν for Ag_2S (inset of **Fig. 2.9 (b)**). The band gaps for Bi_2WO_6 and Ag_2S were estimated as 2.74 eV and 1.1 eV respectively.

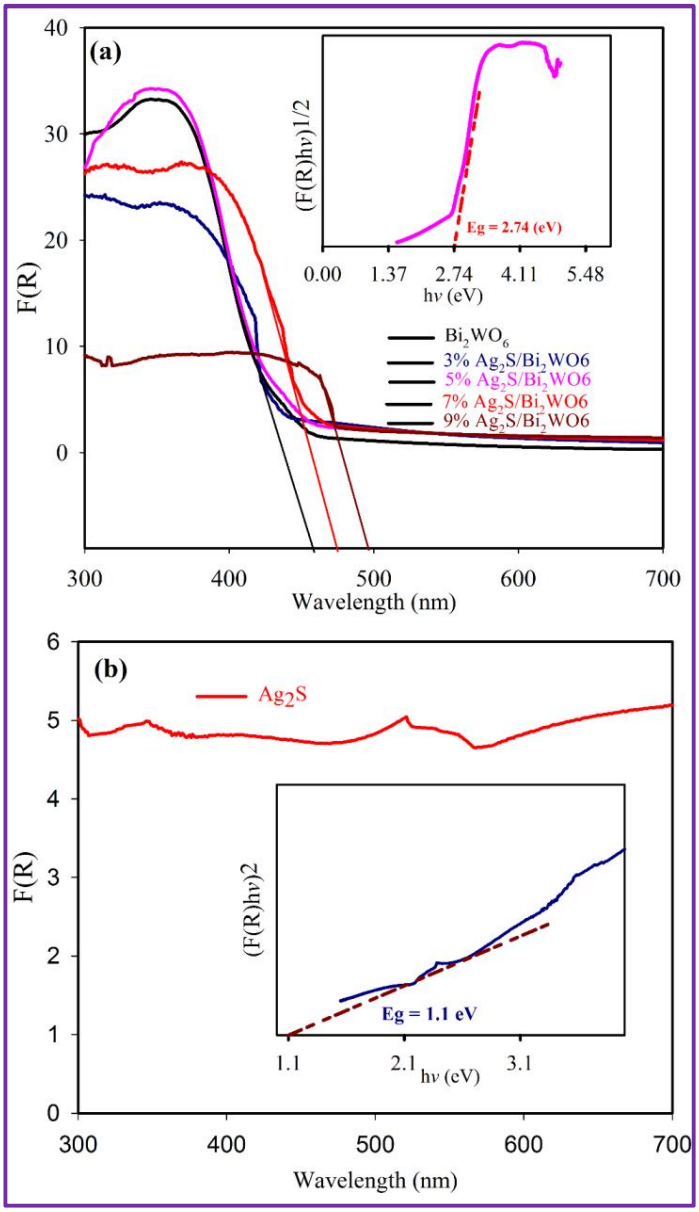

Fig. 2.9: UV–Vis diffuse reflectance spectra of: (a) the pure Bi_2WO_6 and Ag_2S/Bi_2WO_6 composites and (b) the pure Ag_2S catalyst. The insets in the **Fig. 2.9 (a) and Fig. 2.9 (b)** are band gap energies of the pure Bi_2WO_6 and Pure Ag_2S respectively.

2.5.6. Photocatalytic properties

To assess the photocatalytic activity of as prepared samples, RhB was selected as a probe molecule. The characteristic absorption band of RhB at 554 nm was employed to determine the extent of degradation. **Fig. 2.10** displays the photocatalytic performances of all Ag_2S/Bi_2WO_6 heterojunctions with different Ag_2S contents over degradation of RhB (C_t/C_0) under visible light irradiation. As shown in **Fig. 2.10 (b)**, the blank experiment (without photocatalyst) shows that the concentration of RhB remains unchanged even after 50 min of visible light irradiation indicating the significance of photocatalyst. The adsorption of RhB dye by 7% Ag_2S/Bi_2WO_6 was also checked for 50 min and it was found that the adsorption in dark is insignificant. As is shown, the pure mesoporous Bi_2WO_6 exhibit photocatalytic efficiency of 56.5 % in 50 min. The better performance of pure mesoporous Bi_2WO_6 photocatalyst is attributed to the high surface area and mesoporous structure of Bi_2WO_6. The high surface area and mesoporous structure not only provide more active sites and transport paths in photocatalytic reaction, but also improves the contact of photocatalyst with organic pollutants. When Ag_2S and Bi_2WO_6 are combined to construct a heterostructure, the photocatalytic activity of the composites is dramatically enhanced, even though the Ag_2S content is very low. The photocatalytic activities of all Ag_2S/Bi_2WO_6 heterostructures with Ag_2S weight percentage of 3 %, 5%, 7%, and 9% is higher than the bare Bi_2WO_6. The results are listed in **Table 2.2**. The best photocatalytic performance is obtained for 7 % Ag_2S/Bi_2WO_6, for which almost 85% of RhB is degraded in 50 min. The reason for enhanced visible light activity is the formation of heterojunction which results into the generation of natural energy bias at heterojunction with subsequent transfer of photoinduced charge carriers, and therefore, retards the electron-hole recombination. With further increase in Ag_2S content to 9%, the photocatalytic activity decreases but is still higher than bare Bi_2WO_6. Therefore, the optimal content of Ag_2S in Ag_2S/Bi_2WO_6 composite is 7 %. The optimum content of Ag_2S in the heterojunction can be related to two factors: (1) for efficient electron-hole separation the space charge region potential must be certain.[51] When Ag_2S content is above 7% (optimal value), the space charge region might become narrow and lead to the recombination of photoinduced charge carriers, and (2) the loading of Ag_2S leads to decrease in surface area, as discussed in section **2.5.4**. When Ag_2S content is above optimal value, the surface area might decrease substantially leading to decrease in photocatalytic activity. **Fig. 2.10 (a)** displays the absorption spectral changes of the photocatalytic degradation of RhB aqueous solution over 7% Ag_2S/Bi_2WO_6. As can be

seen from the **Fig. 2.10 (a)**, the absorbance of RhB at 554 nm decreases significantly with increase in reaction time accompanied by a slight shift of absorption band towards the blue region which is attributed to the step wise de-ethylation process of RhB into intermediates, as reported in earlier works.[93, 94]

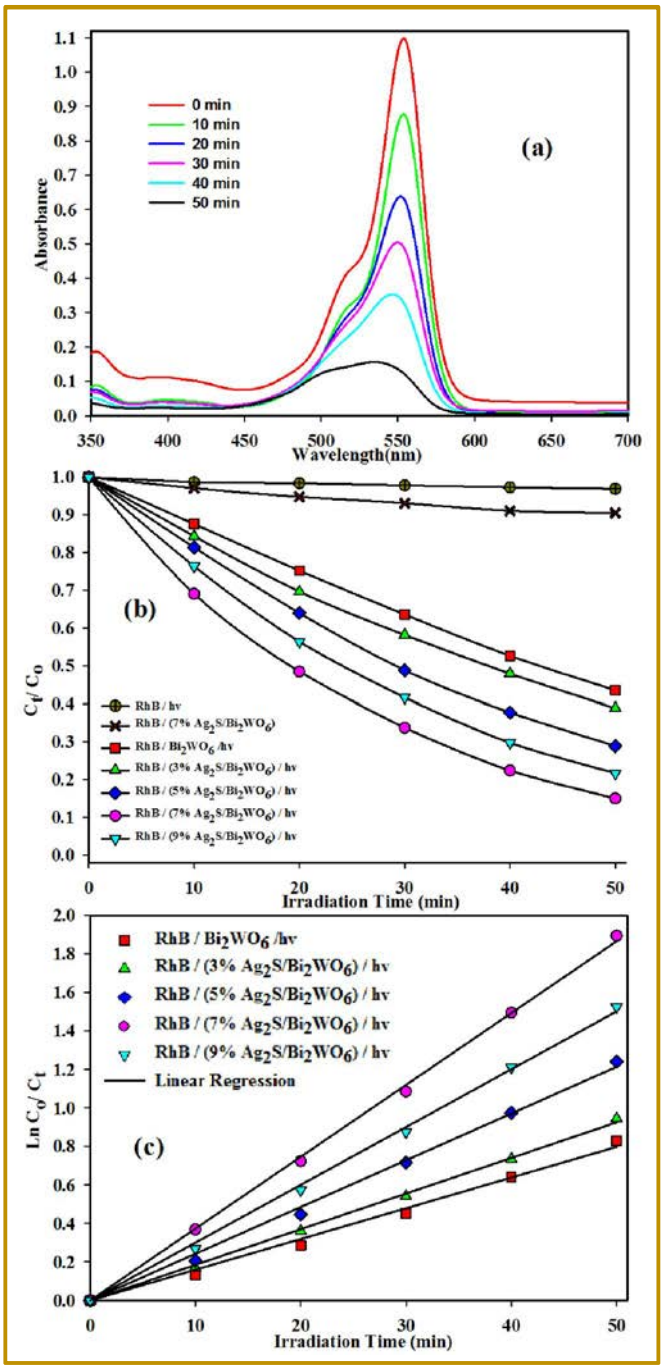

Fig. 2.10: (a) UV–vis spectral changes of the degradation of RhB by the 7% Ag_2S/Bi_2WO_6 catalyst, (b) the degradation efficiency (C_t/C_0) of RhB in presence of pure Bi_2WO_6 and Ag_2S/Bi_2WO_6 composites with different Ag_2S contents, and (c) Rhodamine B decolourization curves of $\ln(C_0/C_t)$ versus irradiation time for different catalysts.

The apparent pseudo first order kinetics model given by the **Equation 2.4** was applied in experiments to understand the reaction mechanism.[95]

$$\ln(C_0/C_t) = K_{app}t \qquad [2.4]$$

where K_{app} is the apparent pseudo-first order reaction constant, and its value for bare Bi_2WO_6 and all heterojunctions was calculated via the first order linear fit data (**Fig. 2.10 (c)).** The results are displayed in **Table 2.2**. From **Table 2.2,** it is clear that photocatalytic activity of 7% Ag_2S/Bi_2WO_6 is 2.4 times higher than the bare Bi_2WO_6 suggesting that Ag_2S/Bi_2WO_6 is an excellent photocatalyst under visible light.

Table 2.2. Pseudo-first-order rate constants (k_{app}) calculated from the plots of ln (C_0/C_t) versus irradiation time for decolorization of RhB over different catalysts, and percent (%) decolorization of RhB for Pure Bi_2WO_6 and Ag_2S/Bi_2WO_6 catalysts with different Ag_2S contents.

Sample	$K_{app}(min^{-1})$	% decolourization
Bi_2WO_6	0.0160	56.42994
3% Ag_2S/Bi_2WO_6	0.0185	61.11649
5% Ag_2S/Bi_2WO_6	0.0243	71.10206
7% Ag_2S/Bi_2WO_6	0.0373	84.96666
9% Ag_2S/Bi_2WO_6	0.0300	78.2553

2.5.7. Proposed Mechanism

The trapping experiments of active species formed during PCO process were carried out to investigate the possible mechanism involved in RhB degradation over 7% Ag_2S/Bi_2WO_6 heterojunction. Benzoquinone (BQ),[96,97] isopropyl alcohol (IPA),[96,98] and ammonium oxalate (AO)[99] were used as superoxide ($^{\bullet}O_2^-$), hydroxyl ($^{\bullet}OH$), and hole (h^+) scavengers, respectively. **Fig. 2.11** displays the effect of different scavengers, and it can be seen clearly that the rate of RhB degradation decreases substantially in presence of AO. However, addition of IPA has no obvious effect on rate of RhB degradation, whereas addition of BQ slightly decreases the photocatalytic performance of 7% Ag_2S/Bi_2WO_6 compared with no scavenger under same conditions. These results indicate that h^+ are the main active species in the RhB degradation over 7% Ag_2S/Bi_2WO_6 system under visible light irradiation.

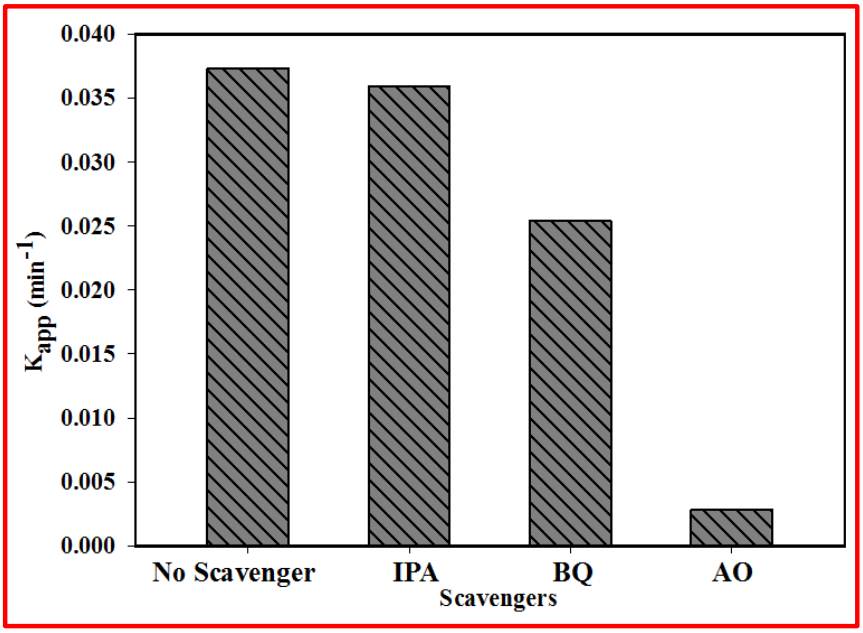

Fig. 2.11: (a) Effect of different scavengers on the degradation of RhB over 7% Ag_2S/Bi_2WO_6 catalyst; BQ = benzoquinone, IA = isopropyl alcohol, AO = ammonium oxalate.

To further confirm that •OH does not play any role, we carried out the Terepthalic acid photoluminescence studies. The PL spectral changes observed during irradiation of Ag_2S/Bi_2WO_6 in a basic TA solution (315 excitation wavelength) are displayed in **Fig. 2.12**. As clear from the figure, no PL signals are observed at 425nm throughout the PCO process indicating that •OH is not formed on the surface of catalyst.

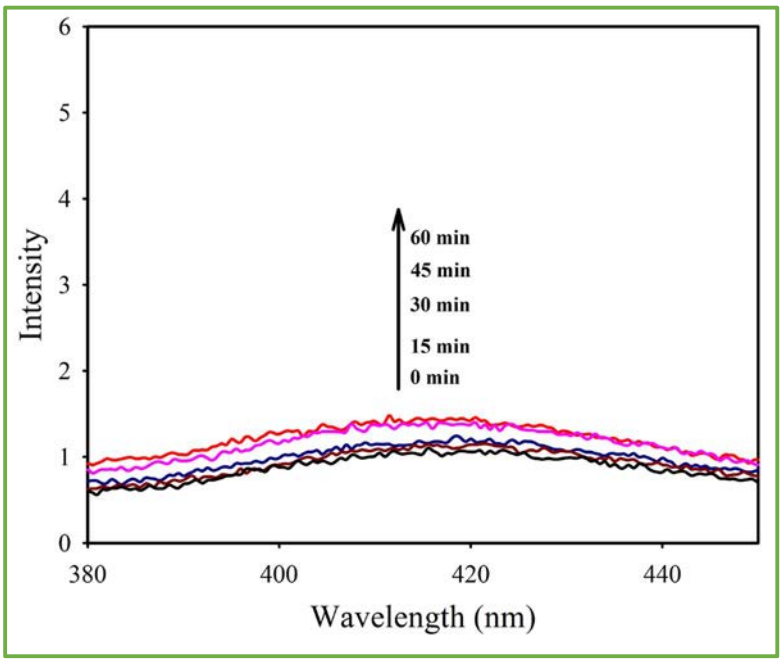

Fig. 2.12: •OH trapping PL spectral changes over 7% Ag_2S/Bi_2WO_6 catalyst in a basic terepthalic acid solution (excitation at 315 nm) with irradiation time.

To ensure that the reactive species originate from the photocatalytic process of catalysts, and not from the sensitization of dye, we selected a colourless molecule, phenol, as a probe. **Fig. 2.13** displays the photocatalytic performances of pure Bi_2WO_6 and 7% Ag_2S/Bi_2WO_6 heterojunctions over degradation of phenol (C_t/C_0) under visible light irradiation. As can be seen from the **Fig. 2.13**, the concentration of phenol decreases with increasing reaction time in presence of both pure Bi_2WO_6 and 7% Ag_2S/Bi_2WO_6. The concentration (C_t/C_0) decreases sharply in presence of 7% Ag_2S/Bi_2WO_6 under visible light irradiation, whereas in case of pure Bi_2WO_6 the decrease in the concentration (C_t/C_0) of phenol is lower than 7% Ag_2S/Bi_2WO_6. Since phenol cannot absorb visible light, it follows directly that reactive species originate from the photocatalytic process of samples under visible light ruling out the possibility of sensitization of dye. The results obtained are in accordance with the results obtained for the degradation of RhB.

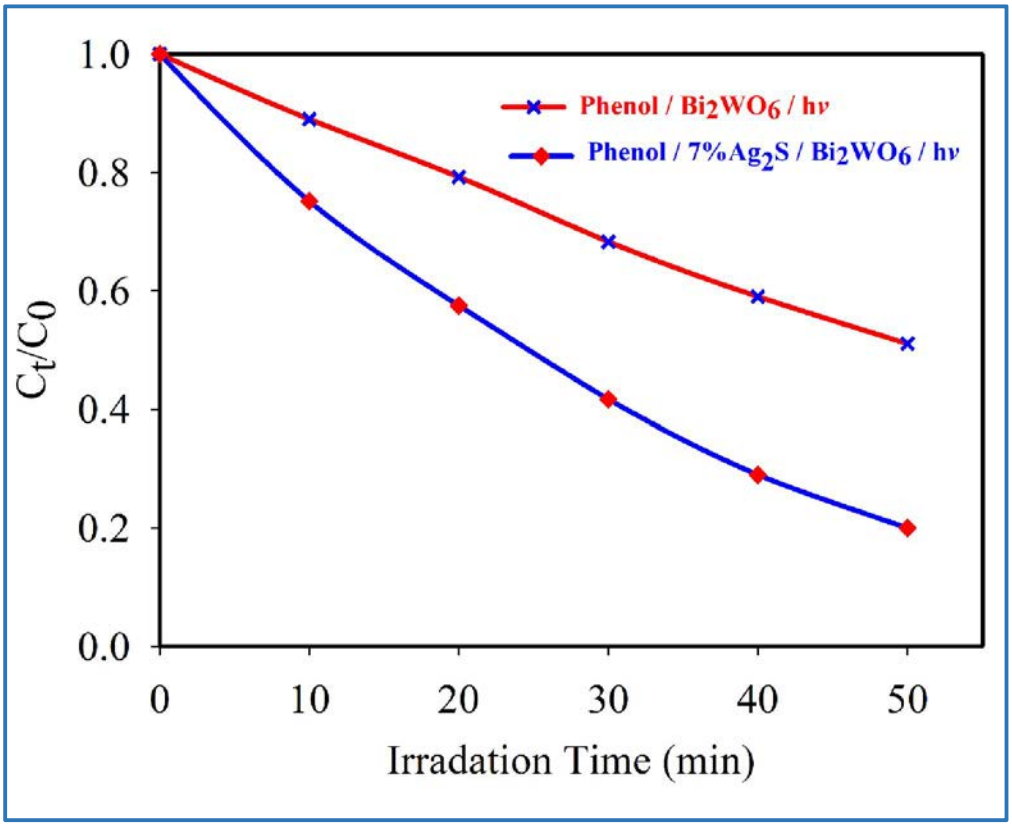

Fig. 2.13: Degradation efficiency (C_t/C_0) of phenol in presence of pure Bi_2WO_6 and 7 % Ag_2S/Bi_2WO_6 composite.

Since Ag_2S loading on the surface of Bi_2WO_6 decreases surface area of Ag_2S/Bi_2WO_6 composite, it can be assumed that large surface area may be responsible for the high photocatalytic activity of bare Bi_2WO_6 but it is not the influencing factor for the

enhancement of visible light activity of Ag_2S/Bi_2WO_6 composites up to 7% loading. Therefore, to analyse the mechanism of improved photocatalytic activity of Ag_2S/Bi_2WO_6 composites, the relative positions of the conduction band and valence band edges of Ag_2S and Bi_2WO_6 were investigated. The relative position of valence band (VB) of Ag_2S and Bi_2WO_6 was evaluated by the empirical formula in **Equation 2.5.**[100]

$$E_{VB} = X - E^c + 0.5E_g \quad [2.5]$$

Where X is the electronegativity of semiconductor expressed as geometric mean of absolute electronegativities of constituent atoms, E^c is the energy of free electrons on hydrogen scale (4.5 eV), and E_g is the band gap energy. The E_{VB} for Ag_2S and Bi_2WO_6 were calculated to be 1.1 eV and 3.23 eV respectively. The relative position of conduction band (CB) of Ag_2S and Bi_2WO_6 were estimated from **Equation 2.6**.

$$E_{CB} = E_{VB} - E_g \quad [2.6]$$

The E_{CB} for Ag_2S and Bi_2WO_6 were calculated to be 0 eV and 0.49 eV respectively.

Based on the results of BET analysis, DRS, Trapping experiments, and TA PL spectra, we presented a schematic diagram to illustrate the photocatalytic reaction mechanism and charge transfer of Ag_2S/Bi_2WO_6 system, as shown in **(Fig. 2.14)**. We propose that under visible light irradiation both Ag_2S and Bi_2WO_6 are excited and generate electron-hole pairs. Since the CB energy level of Ag_2S and Bi_2WO_6 is 0 and 0.49 eV (*vs* SHE), the single electron reduction of O_2 to $^{\bullet}O_2^-$(-0.046 *vs* SHE)[101,102] is not possible. When two semiconductors are in contact, the electrons from less positive conduction band of Ag_2S (0 eV) are injected with high efficiency into more positive conduction band of Bi_2WO_6 (0.49 eV). On the other hand, holes from more positive valence band of Bi_2WO_6 (3.23 eV) are transferred to the less positive VB of Ag_2S (1.1 eV). The photoinduced charge carriers are thus effectively separated at the interface of Ag_2S/Bi_2WO_6. The holes (h^+) on the valence band of Ag_2S cannot react with OH^-/H_2O to form $^{\bullet}OH$ because VB of Ag_2S is more negative (1.1 eV) than that of $^{\bullet}OH/H_2O$ (2.30 eV *vs* SHE) .[51] Hence holes from valence band of Ag_2S migrate to the surface of a photocatalyst where they take part in photocatalytic reaction to mineralize the organic pollutants.

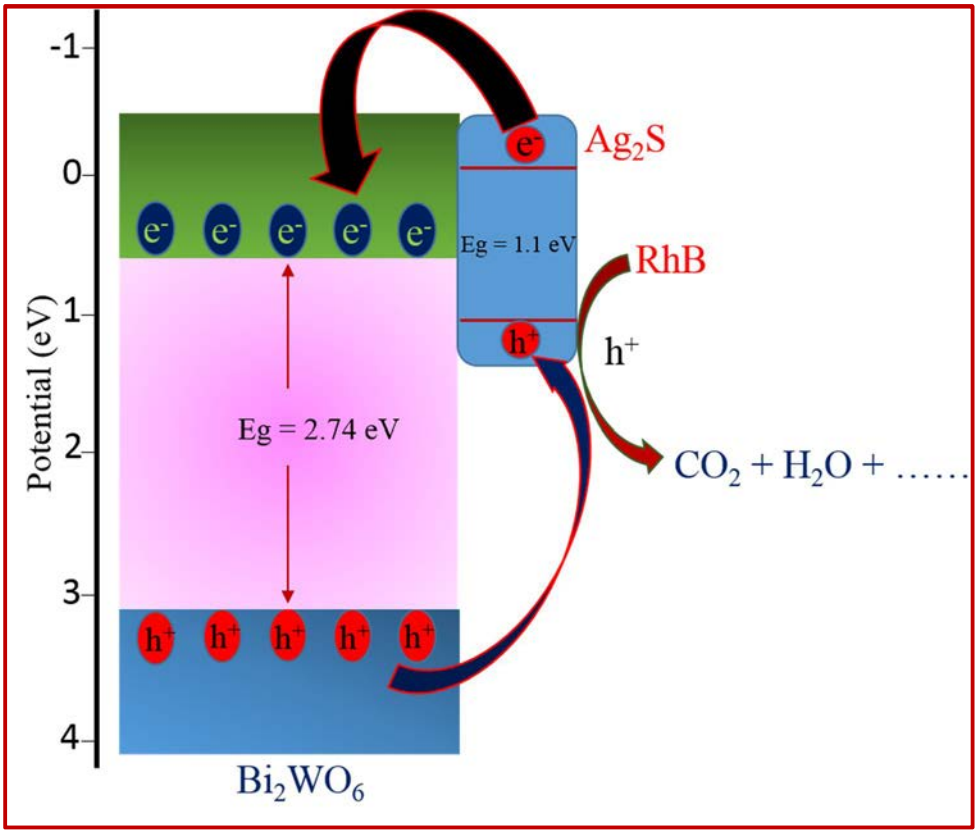

Fig. 2.14: Schematic diagram showing the band structure and separation of photoinduced electron-hole pairs at interface of 7% Ag_2S/Bi_2WO_6 catalyst under visible light irradiation.

Photoluminescence spectra of hierarchically structured bare Bi_2WO6 and 7% Ag_2S/Bi_2WO_6 was carried out to further demonstrate the enhancement of separation of charge carriers. The lower intensity of PL peak represents the lower probability of electron-hole recombination. **Fig. 2.15** presents the PL spectra of bare Bi_2WO_6 and 7% Ag_2S/Bi_2WO_6 with an excitation wavelength of 380 nm. From the **Fig. 2.15**, it is clear that the intensity of PL spectra decreases significantly in 7% Ag_2S/Bi_2WO_6 compared to the bare Bi_2WO_6 indicating that the loading of Ag_2S on Bi_2WO_6 greatly restrains the recombination of photoinduced charge carriers between Bi 6S and O 2P to the empty W4d orbitals.[22]

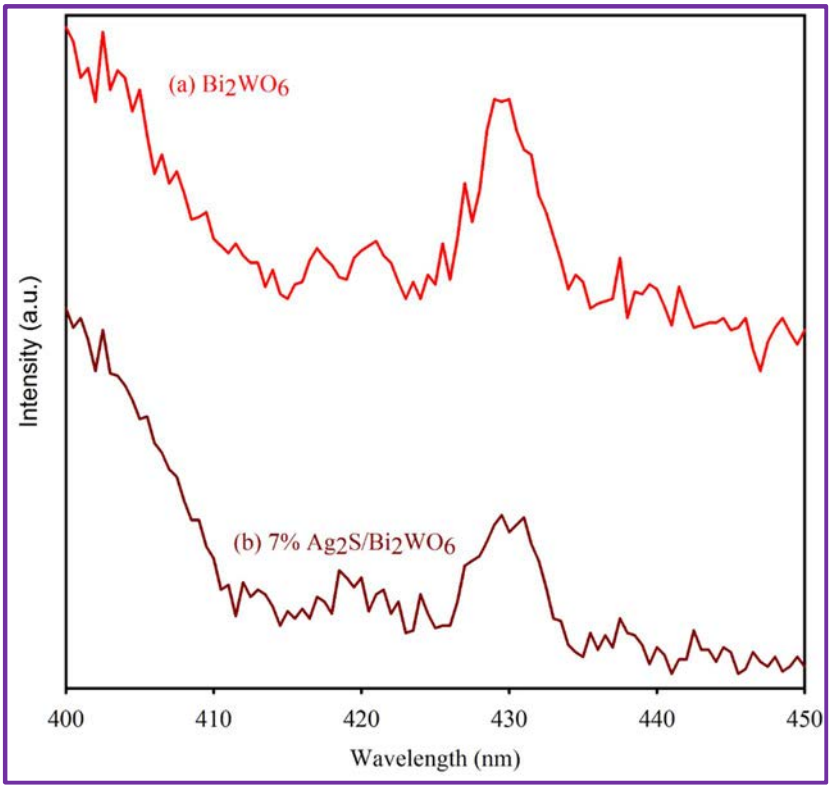

Fig. 2.15: PL spectra of samples: (a) Pure-Bi_2WO_6, and (b) 7% Ag_2S/Bi_2WO_6 (E_x = 380 nm).

2.5.8. Stability of the Catalyst and cycling runs

The stability of silver based compounds has always been a matter of concern,[103] particularly the metal chalcogenides get easily eroded by the photogenerated holes.[104] Therefore, cyclic experiments with 7% Ag_2S/Bi_2WO_6 sample were carried out to determine the stability of a photocatalyst. **Fig. 2.16** displays the results of RhB degradation by 7% Ag_2S/Bi_2WO_6 after 4 repeated cycles. It can be seen from the **Fig. 2.16**, that the degradation of RhB by 7% Ag_2S/Bi_2WO_6 is maintained at 81.3 % even after 4 repeated cycles indicating the high stability of photocatalyst. **Fig. 2.17** presents the Ag3d XPS spectrum and XRD analysis of used 7% Ag_2S/Bi_2WO_6 catalyst after 4 repeated cycles. It is clear from the **Fig. 2.17 (a),** that the Ag3d XPS spectrum of used catalyst is similar to that of fresh catalyst **(Fig. 2.3 (e)),** with no peak detected for metallic Ag in used catalyst after 4 repeated cycles. The XRD analysis of used catalyst **(Fig. 2.17 (b))** after 4 repeated cycles also confirms that the structure and phase of the used catalyst remains intact with no additional peak detected for Ag metal. From these results, it is clear that the Ag_2S/Bi_2WO_6 is a stable photocatalyst under visible light irradiation, and the main reason for the enhanced stability is the transfer of CB electrons from Ag_2S to Bi_2WO_6 which reduces the chances of erosion of catalyst.

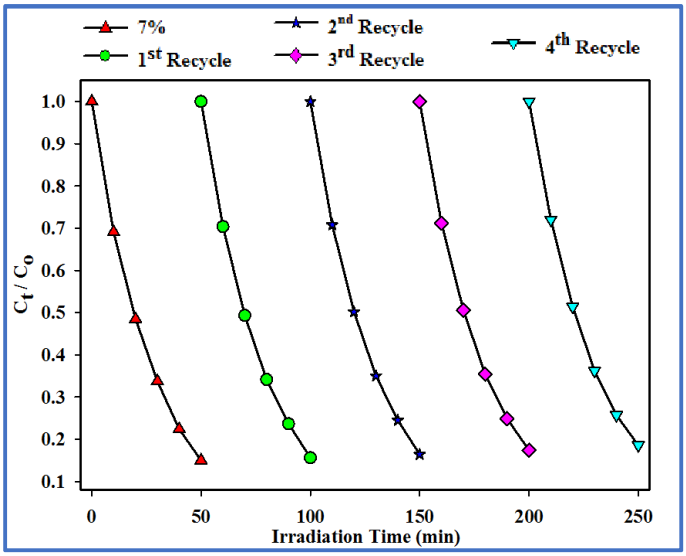

Fig. 2.16: The repeated experiments of photocatalytic degradation of RhB over 7% Ag_2S/Bi_2WO_6 catalyst.

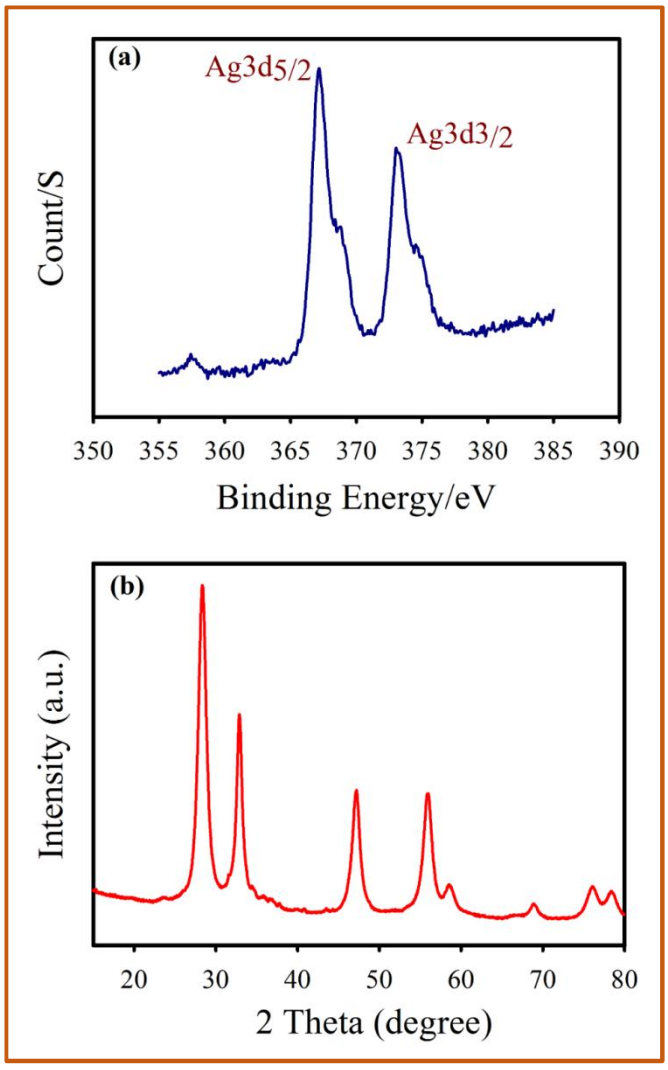

Fig. 2.17: (a) Ag 3d XPS spectra of used 7% Ag_2S/Bi_2WO_6 catalyst after 4 recycling runs, and (b) XRD pattern of used 7% Ag_2S/Bi_2WO_6 catalyst after 4 recycling runs.

2.6. Conclusion

Mesoporous Bi_2WO_6 was modified with Ag_2S by solvothermal method without any surfactant or template. The introduction of Ag_2S extended the photoabsorption range of Bi_2WO_6, and the composite showed red shift compared to the pure Bi_2WO_6. The Ag_2S/Bi_2WO_6 heterostructures showed enhanced photocatalytic activity in the degradation of RhB under visible light irradiation which was 2.4 times higher than the pure Bi_2WO_6. The Ag_2S/Bi_2WO_6 composite even after 4 recycling runs did not show any significant decrease in photocatalytic activity, except for about 4%. The enhanced photocatalytic activity and stability was attributed to the broadening of photoabsorption range and efficient separation of the photoinduced electron-hole pairs as a result of natural energy bias at heterojunction. This study inspires a thought of utilizing visible spectrum efficiently, and simultaneously presents a way to promote separation of photogenerated electron-hole pairs.

References:

[1] B. Aurivillius, *Arkiv for Kemmi* **1** (1949) 463.

[2] I. Etxebarria, J. M. Perez-Mato and P. Boullay, *Ferroelectrics* **17** (2010) 401**.**

[3] J. M. Perez-Mato, M. Aroyo, A. Garcia, P. Blaha, K. Schwarz, J. Schweifer and K. Parlinski, *Phys. Rev. B* **70** (2004) 214111.

[4] J. M. Perez-Mato, P. Blaha, K. Schwarz, M. Aroyo, D. Orobengoa, I. Etxebarria and A. Garcia, *Phys. Rev. B* **77** (2008) 184104.

[5] C. H. Hervoches, A. Snedden, R. Riggs, S. H. Kilcoyne, P. Manuel and P. Lightfoot, *J. Solid State Chem*. **164** (2002) 280.

[6] R. L. Withers, J. G. Thompson and A. D. Rae, *J. Solid State Chem.* **94** (1991) 404.

[7] S. S. Yao, J. Y. Wei, B. B. Huang, S. Y. Feng, X. Y. Zhang, X. Y. Qin, P. Wang, Z. Y. Wang, Q. Zhang, X. Y. Jing and J. Zhan, *J. Solid State Chem.* **182** (2009) 236.

[8] Y. F. Sun, Y. Xie, C. Z. Wu, S. D. Zhang and S. S. Jiang, *Nano Res.* **3** (2010) 620.

[9] H. Huang, S. Wang, Y. Zhang and P. K. Chu, *RSC Adv.* **4** (2014) 41219.

[10] N. Baux, R. N. Vannier, G. Mairesse and G. Nowogrocki, *Solid State Ionics* **91** (1996) 243.

[11] N. Kim, R. N. Vannier and C. P. Grey, *Chem. Mater.* **17** (2005) 1952.

[12] R. Rangel, P. Bartolo-Perez, A. Gomez-Cortetz, G. Diaz and D. H. Galvan, *Surf. Rev. Lett.* **9** (2002) 1779.

[13] H. F. Cheng, B. B. Huang, Y. Dai, X. Y. Qin, X. Y. Zhang, Z. Y. Wang and M. H. Jiang, *J. Solid State Chem*. **182** (2009) 2274.

[14] M. Ge, Y. F. Li, L. Liu, Z. Zhou and W. Chen, *J. Phys. Chem. C* **115** (2011) 5220.

[15] A. Kudo, K. Omori and H. Kato, *J. Am. Chem. Soc.* **121** (1999) 11459.

[16] L. S. Zhang, H. L. Wang, Z. G. Chen, P. K. Wong and J. S. Liu, *Appl. Catal. B* **106** (2011) 1.

[17] F. Amano, A. Yamakata, K. Nogami, M. Osawa and B. Ohtani, *J. Am. Chem. Soc.* **130** (2008) 17650.

[18] G. S. Li, D. Q. Zhang, J. C. Yu and M. K. H. Leung, *Environ. Sci. Technol.* **44** (2010) 4276.

[19] L. Wu, J. H. Bi, Z. H. Li, X. X. Wang and X. Z. Fu, *Catal. Today* **131** (2008) 15.

[20] Z. J. Zhang, W. Z. Wang, M. Shang and W. Z. Yin, *J. Hazard. Mater.* **177** (2010) 1013.

[21] S. Shamaila, A. K. L. Sajjad, F. Chen and J. L. Zhang, *Appl. Catal. B* **94** (2010) 272.

[22] J. Ren, W. Z. Wang, S. M. Sun, L. Zhang and J. Chang, *Appl. Catal. B* **92** (2009) 50.

[23] M. R. Hoffmann, S. T. Martin, W. Choi and D. W. Bahemann, *Chem. Rev.* **95** (1995) 69.

[24] X. Wang, J. C. Yu, C. Ho, Y. Hou and X. Fu, *Langmuir* **21** (2005) 2552.

[25] L. S. Zhang, W. Z. Wang, Z. G. Chen, L. Zhou, H. L. Xu and W. Zhu, *J. Mater. Chem.* **17** (2007) 2526.

[26] L. W. Zhang, Y. J. Wang, H. Y. Cheng, W. Q. Yao and Y. F. Zhu, *Adv. Mater.* **21** (2009) 1286.

[27] D. J. Wang, Y. Z. Zhen, G. L. Xue, F. Fu, X. M. Liu and D. S. Li, *J. Mater. Chem. C* **1** (2013) 4153.

[28] H. Fu, C. Pan, W. Yao and Y. Zhu, *J. Phys. Chem. B* **109** (2005) 22432.

[29] D. Wu, H. Zhu, C. Zhang and L. Chen, *Chem. Commun.* **46** (2010) 7250.

[30] F. Amano, K. Nogami, R. Abe and B. Ohtani, *Chem. Lett.* **36** (2007) 1314.

[31] H. Wang, J. M. Song, H. Zhang, F. Gao, S. J. Zhao and H. Q. Hu, *Mater. Res. Bull.* **47** (2012) 1919.

[32] S. G. Liu and J. G. Yu, *J. Solid State Chem.* **181** (2008) 1048.

[33] Z. Chen, L. W. Qian, J. Zhu, Y. P. Yuan and X. F. Qian, *CrystEngComm* **12** (2010) 2100.

[34] Y. Tian, G. M. Hua, W. Xu, N. Li, M. Fang and L. D. Zhang, *J. Alloys Compd.* **509** (2011) 724.

[35] H. Bai and X. Liu, *Mater. Lett.* **64** (2010) 341.

[36] L. Y. Yang, G. P. Feng and T. X. Wang, *Mater. Lett.* **64** (2010) 1647.

[37] T. H. Guo, Y. Liu, Y. C. Zhang and M. Zhang, *Mater. Lett.* **65** (2011) 639.

[38] Y. X. Zhou, L. Tong, X. H. Zeng and X. B. Chen, *New J. Chem.* **38** (2014) 1973.

[39] Y. Peng, Q. G. Chen, D. Wang, H. Y. Zhoua and A. W. Xu, *CrystEngComm* **17** (2015) 569.

[40] C. Zhang and Y. Zhu, *Chem. Mater.* **17** (2005) 3537.

[41] H. Fu, L. Zhang, W. Yao and Y. Zhu, *Appl. Catal. B* **66** (2006) 100.

[42] S. Zhang, C. Zhang, Y. Man and Y. Zhu, *J. Solid State Chem.* **179** (2006) 62.

[43] J. Yu, J. Xiong, B. Cheng, Y. Yu and J. Wang, *J. Solid State Chem.* **178** (2005) 1968.

[44] Z. Zhang, W. Wang, L. Wang and S. Sun, *Appl. Mater. Interfaces* **4** (2012) 593.

[45] J. Cao, B. Xu, H. Lin, B. Luo and S. Chen, *Chem. Eng. J.* **185–186** (2012) 91.

[46] Y. F. Hou, S. J. Liu, J. H. Zhang, X. Cheng and Y. Wang, *Dalton Trans.* **43** (2014) 1025.

[47] Y. Guo, G. Zhang, J. Liua and Y. Zhang, *RSC Adv.* **3** (2013) 2963.

[48] Y. Zheng, K. Lv, X. Li, K. Deng, J. Sun, L. Chen and L. Cui, *Chem. Eng. Technol.* **34** (2011) 1630.

[49] J. Xia, J. Di, S. Yin, H. Xu, J. Zhang, Y. Xu, L. Xu, H. Li and M. Jia, *RSC Adv.* **4** (2014) 82.

[50] Z. Zhang, W. Wang and L. Zhang, *Dalton Trans.* **42** (2013) 4579.

[51] D. Wang, L. Guo, Y. Zhen, L. Yue, G. Xue and F. Fu, *J. Mater. Chem. A* **2** (2014) 11716.

[52] L. Zhang, K. H. Wong, Z. Chen, J. C. Yu, J. Zhao, C. Hu, C. Y. Chan and P. K. Wong, *Appl. Catal. A* **363** (2009) 221.

[53] J. Low, J. Yu, Q. Li and B. Cheng, *Phys. Chem. Chem. Phys.* **16** (2014) 1111.

[54] Y. S. Xu, Z. J. Zhang and W. D. Zhang, *Dalton Trans.* **43** (2014) 3660.

[55] Y. Li, J. Liu, X. Huang and J. Yu, *Dalton Trans.* **39** (2010) 3420.

[56] H. Huang, S. Wang, N. Tian and Y. Zhang, *RSC Adv.* **4** (2014) 5561.

[57] Z. Zhang, W. Wang, D. Jiang and J. Xu, *Appl. Surf. Sci.* **292** (2014) 948.

[58] S. H. Chen, Z. Yin, S. L. Luo, X. J. Li, L. X. Yang and F. Deng, *Appl. Surf. Sci.* **259** (2012) 7.

[59] F. Duan, Y. Zheng and M. Chen, *Appl. Surf. Sci.* **257** (2011) 1972.

[60] 24 X. P. Lin, T. Huang, F. Q. Huang, W. D. Wang and J. L. Shi, *J. Mater. Chem.* **17** (2007) 2145.

[61] S. S. Qian, C. S. Wang, W. J. Liu, Y. H. Zhu, W. J. Yao and X. H. Lu, *J. Mater. Chem.* **21** (2011) 4945.

[62] J. Jiang, X. Zhang, P. B. Sun and L. Z. Zhang, *J. Phys. Chem. C* **115** (2011)20555.

[63] G. P. Dai, J. G. Yu and G. Liu, *J. Phys. Chem. C* **115** (2011) 7339.

[64] J. Bisquert, D. Cahen, G. Hodes, S. Ruhle and A. Zaban, *J. Phys. Chem. B* **108** (2004) 8106.

[65] J. N. Clifford, E. Martinez-Ferrero, A. Viterisi and E. Palomares, *Chem. Soc. Rev.* **40** (2011) 1635.

[66] A. Tubtimtae, K. L. Wu, H. Y. Tung, M. W. Lee and G. J. Wang, *Electrochem. Commun.* **12** (2010) 1158.

[67] J. J. Wu, R. C. Chang, D. W. Chen and C. T. Wu, *Nanoscale* **4** (2012) 1368.

[68] Z. D. Meng, T. Ghosh, L. Zhu, J. G. Choi, C. Y. Park and W. C. Oh, *J. Mater. Chem.* **22** (2012) 16127.

[69] X. Yi, H. S. Hwan, K. Y. Nam, Y. S. Hwa and C. S. Oh, *Nanotechnology* **21** (2010) 015703.

[70] K. Nagasuna, T. Akita, M. Fujishima and H. Tada, *Langmuir* **27** (2011) 7294.

[71] I. Hwang and K. Yong, *ChemPhysChem* **14** (2013) 364.

[72] Y. X. Li, G. Chen, C. Zhou and J. X. Sun, *Chem. Commun.* (2009) 2020.

[73] R. Vogel, P. Hoyer and H. Weller, *J. Phys. Chem.* **98** (1994) 3183.

[74] S. Liu, X. T. Wang, W. X. Zhao, K. Wang, H. X. Sang and Z. He, *J. Alloys Compd.* **568** (2013) 84.

[75] S. H. Shen, L. J. Guo, X. B. Chen, F. Ren and S. S. Mao, *Int. J. Hydrogen Energy* **35** (2010) 7110.

[76] Y. P. Du, B. Xu, T. Fu, M. Cai, F. Li, Y. Zhang and Q. B. Wang, *J. Am. Chem. Soc.* **132** (2010) 1470.

[77] X. Wang, S. Zhan, Y. Wang, P. Wang, H. Yu, J. Yu and C. Hu, *J. Colloid Interface Sci.* **422** (2014) 30.

[78] J. Wu, F. Duan, Y. Zheng and Y. Xie, *J. Phys. Chem. C* **111** (2007) 12866.

[79] M. Penza, M. A. Tagliente, L. Mirenghi, C. Gerardi, C. Martucci and G. Cassano, *Sens. Actuators B* **50** (1998) 9.

[80] S. Bai, X. P. Shen, H. W. Lv, G. X. Zhu, C. L. Bao and Y. X. Shan, *J. Colloid Interface Sci.* **405** (2013) 1.

[81] M. Pang, J. Hu and H. C. Zeng, *J. Am. Chem. Soc.* **132** (2010) 10771.

[82] H. Zhang, G. Wang, D. Chen, X. Lv and J. Li, *Chem. Mater.* **20** (2008) 6543.

[83] L. Qi, J. Yu and M. Jaroniec, *Phys. Chem. Chem. Phys.* **13** (2011) 8915.

[84] H. G. Yu, R. Liu, X. F. Wang, P. Wang and J. G. Yu, *Appl. Catal. B* **111–112** (2012) 326.

[85] G. I. N. Waterhouse, G. A. Bowmaker and J. B. Metson, *Phys. Chem. Chem. Phys.* **3** (2001) 3838.

[86] D. Jiang, L. Chen, J. Xie and M. Chen, *Dalton Trans.* **43** (2014) 4878.

[87] J. P. Xiao, Y. Xie, R. Tang and W. Luo, *J. Mater. Chem.* **12** (2002) 1148.

[88] M. A. Butler, *J. Appl. Phys.* **48** (1977) 1914.

[89] G. Zhao, S. Liu, Q. Lu, F. Xu and H. Sun, *J. Alloys Compd.* **578** (2013) 12.

[90] C. Bhattacharya, H. C. Lee and A. J. Bard, *J. Phys. Chem. C* **117** (2013) 9633.

[91] F. Amano, K. Nogami and B. Ohtani, *Catal. Commun.* **20** (2012) 12.

[92] H. Fu, S. Zhang, T. Xu, Y. Zhu and J. Chen, *Environ. Sci. Technol.* **42** (2008) 2085.

[93] J. Fu, Y. L. Tian, B. B. Chang, F. N. Xi and X. P. Dong, *J. Mater. Chem.* **22** (2012) 21159.

[94] J. X. Xia, S. Yin, H. M. Li, H. Xu, L. Xu and Y. G. Xu, *Dalton Trans.* **40** (2011) 5249.

[95] C. H. Wu, H. W. Chang and J. M. Chern, *J. Hazard. Mater.* **137** (2006) 336.

[96] G. T. Li, K. H. Wong, X. W. Zhang, C. Hu, J. C. Yu, R. C. Y. Chan and P. K. Wong, *Chemosphere* **76** (2009) 1185.

[97] M. C. Yin, Z. S. Li, J. H. Kou and Z. G. Zou, *Environ. Sci. Technol.* **43** (2009) 8361.

[98] L. S. Zhang, K. H. Wong, H. Y. Yip, C. Hu, J. C. Yu, C. Y. Chan and P. K. Wong, *Environ. Sci. Technol.* **44** (2010) 1392.

[99] N. Zhang, S. Q. Liu, X. Z. Fu and Y. J. Xu, *J. Phys. Chem. C* **115** (2011) 9136.

[100] X. Zhang, L. Z. Zhang, T. F. Xie and D. J. Wang, *J. Phys. Chem. C* **113** (2009) 7371.

[101] X. Wang, S. Li, Y. Ma, H. Yu and J. Yu, *J. Phys. Chem. C* **115** (2011) 14648.

[102] A. J. Bard, R. Parsons, J. Jordan, *Standard Potentials in Aqueous Solutions*, CRC Press, New York (1985).

[103] O. Mehraj, N. A. Mir, B. M. Pirzada, S. Sabir and M. Muneer, *J. Mol. Cat. A*: *Chem.* **395** (2014) 16

[104] J. Ran, J. Yu and M. Jaroniec, *Green Chem.* **13** (2011) 2708.